Segmentation of the skull in MRI volumes using deformable model and taking the partial volume effect into account

Hilmi Rifai[a,*], Isabelle Bloch[a], Seth Hutchinson[a,b], Joe Wiart[c], Line Garnero[d]

[a]Ecole Nationale Supérieure des Télécommunications, Département TSI, CNRS URA 820, 46 Rue Barrault, 75013 Paris, France
[b]University of Illinois at Urbana-Champaign, 2017 Beckman Institute, 405 North Matthews Avenue, Urbana, IL 61801, USA
[c]CNET/France Telecom, Issy les Moulineaux, France
[d]LENA, CNRS URA 654, Hôpital La Salpêtrière, Paris, France

Abstract

Segmentation of the skull in medical imagery is an important stage in applications that require the construction of realistic models of the head. Such models are used, for example, to simulate the behavior of electro-magnetic fields in the head and to model the electrical activity of the cortex in EEG and MEG data. In this paper, we present a new approach for segmenting regions of bone in MRI volumes using deformable models. Our method takes into account the partial volume effects that occur with MRI data, thus permitting a precise segmentation of these bone regions. At each iteration of the propagation of the model, partial volume is estimated in a narrow band around the deformable model. Our segmentation method begins with a pre-segmentation stage, in which a preliminary segmentation of the skull is constructed using a region-growing method. The surface that bounds the pre-segmented skull region offers an automatic 3D initialization of the deformable model. This surface is then propagated (in 3D) in the direction of its normal. This propagation is achieved using level set method, thus permitting changes to occur in the topology of the surface as it evolves, an essential capability for our problem. The speed at which the surface evolves is a function of the estimated partial volume. This provides a sub-voxel accuracy in the resulting segmentation. © 2000 Elsevier Science B.V. All rights reserved.

1. Introduction

The segmentation of the skull in medical images is an important step toward complete segmentation of the tissue in the human head, the latter being an indispensable step in the construction of a realistic model of the head. Such models are used for numerical simulation of the behavior of electro-magnetic fields in tissues (Wiart and Mittra, 1996) as well as for the study of electrical activity in the cerebral cortex in EEG (electroencephalography) and MEG (magnetoencephalography) data (Marin, 1997). In these applications, each component of the model is characterized by the electro-magnetic properties of the tissue being modeled. The electro-magnetic properties of the skull are

such that any realistic model of the head must take bone regions into account. Although simplified models of the head are sometimes used in these endeavors (e.g., nested spheres (Meijs et al., 1987)), the construction of more realistic models is currently of growing importance. Medical imagery can be exploited for this task, since such imagery reveals both the structure and the composition of the tissue in the region under study (Jensen and Rahmat-Samii, 1995). The segmentation of the skull is also important in approaches which study various neurological disorders by aligning and normalizing a volumetric image of the intracranial cavity with respect to size and shape. The segmented boundary of the skull can be exploited in this normalization process, since it directly defines the shape and size of the intracranial cavity.

Of the currently available imaging modalities, CT data are the best suited to the problem of segmentation of the skull (Subsol, 1995). Nevertheless, for the following

*Corresponding author. Tel.: +33-145-81-7069; fax: +33-145-81-3794.
E-mail address: rifai@tsi.enst.fr (H. Rifai).

reasons we address the problem of segmenting bone regions in MRI volumes rather than in CT data:

- The acquisition of MRI data is not harmful to the subject (Wehli et al., 1988) (unlike CT imaging). This facilitates the acquisition of complete scans of the head at high resolution, without the risk of exposure to high doses of radiation.
- MRI data are well suited to the segmentation of soft tissues, and of the cerebral cortex in particular. Accurately representing these tissues in the model is very important due to their electro-magnetic properties (Jensen and Rahmat-Samii, 1995). Thus, with MRI data, an individual model comprising all of the structures of the head may be constructed from data obtained by a single acquisition.

A number of factors complicate the problem of segmenting the skull in MRI volumes. These include partial volume effects, variable topology of the skull between individuals, regions of the skull with very high curvature, and regions of the skull whose thickness is small relative to voxel size. In this paper, we describe a deformable model approach that deals with these problems. We begin in Section 2 with a description of our problem and the motivations for using deformable models. In Section 2 we also address issues related to the automatic initialization of the method. In Section 3, we give a brief review of the level set formalism for front propagation, which we use to compute the evolution of the deformable model. In Section 4 we describe our new approach for taking into account partial volume effects; we first review some related approaches, and then describe how we estimate, and subsequently incorporate into the surface evolution equations, the partial volume information. Section 5 deals with a number of implementation issues related to parameter selection. In Section 6, we present several experimental results and evaluations, for both simulated MRI data (so that we can draw comparisons to known ground truth segmentations) and for real MRI data. Section 7 presents conclusions and perspectives.

We conclude this section by presenting some background on segmenting bone regions in MRI data, and then giving a brief overview of our approach.

1.1. Background

Very little research has been devoted to the problem of segmentation of the skull in MRI data, since CT images are typically used for the purpose of segmenting bone regions. Soltanian-Zadeh and Windham (1997) use a multi-scale approach to extract the internal and external contours of the skull from a CT image, with the goal of registering this segmentation to an MRI volume. Another approach, developed by Studholme et al. (1996), segments bone in the MRI data using a rigid registration of a CT volume with an MRI volume from the same subject. In other research, bone is segmented directly in the MRI volumes in order to forego entirely the acquisition of CT

images. Held et al. (1997) define classes, including a scalp-bone class, and use a Markov random field (MRF) approach to segment the classes in the MRI volume. Heinonen et al. (1997) use thresholding and region growing to segment bone in MRI volumes.

The results of these previous methods have not always been satisfying. With MRF-based methods (e.g., Held et al., 1997), it is not possible to guarantee that continuous bounding contours will be obtained. For this reason, a stage in which contours are connected is proposed in (Soltanian-Zadeh and Windham, 1997), but for the case of CT images. The case of MRI data is more complicated, since partial volume effects make the segmentation of certain bone regions, for example the ocular globes, more difficult. This difficulty is mentioned in (Heinonen et al., 1997), where certain regions of the skull were not recovered. To date, none of the methods that have been proposed deal with partial volumes effects, consideration of which is indispensable for a precise segmentation of the skull. We note, finally, that the choice of a multi-modal approach (CT/MRI) does not seem practical for the reasons mentioned above.

1.2. The proposed approach

The originality of our approach lies in the use of a 3D deformable model with variable topology to segment the skull in MRI volumes, and in how we take into account partial volume effect to formulate the speed function of the model.

Deformable contour models (sometimes referred to as active contour models) were first introduced in the computer vision community in (Kass et al., 1988). The basic approach when using deformable models for segmentation can be summarized as follows. First, an initial surface is computed; this can be done automatically or manually. This surface is then deformed subject to artificial forces that are derived from the objectives of the segmentation process. In general, a combination of two forces is used: one force that constrains the final surface to have desired smoothness properties, and one force that constrains the final surface to fit the observed data. The exact definition of these forces, and their relative weighting, has been the subject of much research (McInerney and Terzopoulos, 1996).

In our approach, the use of a deformable model guarantees that the resulting regions in the segmentation will be enclosed by connected contours. The 3D initialization of the model is made automatically using a region-growing technique. This allows us to forego manual initialization, which can be very difficult due to the topological complexity of the skull. Furthermore, we present a method for taking into account partial volume effect in a band surrounding the model at each iteration of its propagation. The speed function of the model, which completely determines the surface deformation, is then defined to be a function of this partial volume estimate; this enables a

sub-voxel segmentation. We implement the surface deformation using level set method (Osher and Sethian, 1988). This permits changes in the topology of the surface as it evolves, a capability that is advantageous during segmentation of the skull, whose topology varies between individuals. Finally, we note that the level set formulation on which the propagation of our deformable surface is based, in conjunction with our method for exploiting partial volume information, permits the realization of a sub-voxel segmentation of bone regions.

In what follows, Section 2 describes the deformable model formalism that we use for segmenting the skull, as well as the preprocessing stages. Section 3 briefly reviews front propagation using level sets. In Section 4, we describe the partial volume estimation and model speed calculation. Section 5 describes the choice of several different parameters of our model. Section 6 presents results of the segmentation of the skull in simulated and real MRI volumes. Section 7 presents conclusions and perspectives.

2. Segmentation of the skull using deformable model

2.1. Deformable models in medical image processing

Deformable models are frequently used in medical image processing, and have been widely applied to problems including segmentation, tracking and registration. For example, Clarysse et al. (1997) use deformable surfaces to study the movement of the surface of the left ventricle of the heart. Davatzikos and Bryan (1996) use an active contour to obtain a mathematical representation of the cortex. Gee et al. (1993) use an elastic atlas to register cerebral images. Fok et al. (1996) segment nerve cells using active contours. These are just a few examples. A more detailed analysis of the use of deformable models in medical image processing can be found in (McInerney and Terzopoulos, 1996).

Deformable models offer several advantages for the segmentation of anatomical organs, including the following.

- Deformable models can be used to obtain closed and smooth contours, even if the images are noisy (Rueckert et al., 1997).
- Certain deformable models are topology preserving (e.g., Mangin, 1995), while others allow changes in the topology without introducing difficulties related to parameterization (Caselles et al., 1997).
- Some deformable models (e.g., using Fourier descriptors (Staib and Duncan, 1992)) allow to obtain an analytic mathematical description of the segmented contour rather than a set of points.
- Deformable models can be used for the 3D reconstruction of anatomical organs (Bardinet et al., 1994).
- Specific models exist that can be adapted to the

segmentation of different anatomical organs (Lobregt and Viergever, 1995).
- Control of the model parameters (e.g., elasticity and curvature) can be local (as, for example, with snakes (Kass et al., 1988)), or global (as, for example, with hyperquadrics (Cohen and Cohen, 1994)).

2.2. Characteristics of the model

The choice of a model must take into account several considerations. In this section, we briefly discuss a number of factors that motivated us in our selection of a specific deformable model approach.

The skull is topologically complex, especially in the temporal region. This implies that the deformable model must be capable of representing complex shapes. Deformable models with global shape control (as, for example, with hyperquadrics (Cohen and Cohen, 1994)) are not suitable for our problem. The deformable model that we use is deformed by local external and internal forces. This choice offers local control on the shape of the model, thus permitting more flexibility in the deformation process.

The topology of the skull is not fixed. In effect, the inter-individual variations in certain regions (e.g., the fatty regions in the upper part of the skull) necessitate the use of a deformable model that allows changes in topology. So, the propagation of the model is carried out using level sets technique, which (unlike classical snakes approach) permits topology changes without parametrisation problems.

The complexity of the skull poses a problem for the 3D initialization of the model. Since manual initialization is difficult for the user, it is necessary that the initialization be automatic. We begin with a pre-segmentation of the skull using a region-growing technique. The external surface of the pre-segmented region offers a 3D automatic initialization of the deformable model. The variation of topology during the propagation of the model can eliminate tunnels and holes which can appear with region growing segmentation.

Certain parts of the skull are thin compared to the resolution currently available in MRI data. This is the case for the ocular globes as well as for certain portions of the upper region of the skull. Such problems manifest themselves as partial volume effects (i.e., voxels will contain more than a single type of material), and impose the requirement that the deformable model be capable of providing a sub-voxel segmentation of bone regions. With level sets technique, the deformable model is estimated as the zero level of a hypersurface. This estimation, when combined with partial volume estimation, offers a sub-voxel precision unlike discrete approaches used classically in deformable models (Lobregt and Viergever, 1995).

There exist various interfering contours in the bone regions. These contours are essentially due to noise and to partial volume effects. As we will describe below, we have chosen to define the forces that determine the model deformation to be a function of (i) the information

contained in the regions to be segmented (Cohen et al., 1993) (based on the partial volume of bone in each voxel) and (ii) on the shape of the contours themselves (which is a classical approach used with deformable models (Kass et al., 1988)). This choice provides the advantages of better taking into account the composition of the voxels, and of providing a sub-voxel segmentation of the bone regions.

In T1-weighted MRI, the CSF (cerebro-spinal fluid) and the bone are connected regions with comparable grey levels (Wehli et al., 1988). To isolate the CSF and to initialize the model, we begin with a preprocessing stage, which we now describe.

2.3. Initializing the deformable model

The deformable model is initialized during a preprocessing step. This preprocessing comprises two stages: a morphological segmentation of the brain followed by a pre-segmentation of the skull.

2.3.1. Morphological segmentation of the brain

We begin by performing a morphological segmentation of the brain (Géraud et al., 1995a,b). The goal of this stage is to identify the CSF that exists in the cortex folds, subsequently preventing the deformable model from segmenting the CSF as bone regions of the head. This process consists of the following main steps:

1. Two thresholds, s_{inf} and s_{sup}, are selected, to isolate the brain from the non-signal region that corresponds to bone and the high-signal regions that correspond to blood vessels.
2. Binary erosion of radius 4 mm is used to separate the brain from the skin.
3. The largest connected component, which corresponds to the brain, is extracted.
4. Binary dilation of radius 4 mm is used to reconstruct the brain.
5. Binary closure of radius 2 mm is used to close the cortex folds and thus to isolate the CSF.

Fig. 1 shows an example of a slice of MRI volume and the result of the segmentation of the brain. The deformable model that we use f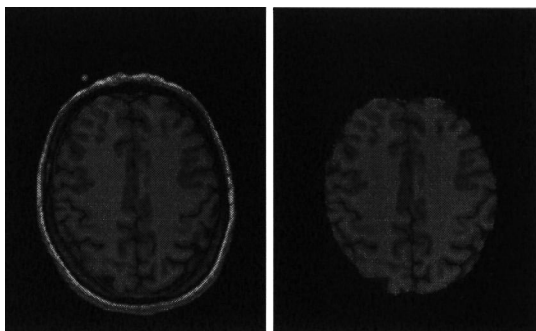or the segmentation of the skull will be repelled by the region corresponding to the segmented brain, thus preventing the model from penetrating into the cortex folds.

2.3.2. Pre-segmentation of the skull

The goal of the pre-segmentation is to furnish a 3D automatic initialization of the deformable model as well as to determine the statistics for the bone regions. The pre-segmentation is achieved by a region growing, as follows. The region is initialized to contain those voxels that are adjacent to the segmented brain, and that have grey value less than s_{inf}. This region is grown by successively adding 26-connected voxels whose grey level is less than the threshold value s_{inf} (described above). Using the resulting region, we calculate the mean μ_{bone}, and the standard deviation σ_{bone}, of the pre-segmented skull region. These two parameters will be used during the calculation of the speed of the deformable model (described in Section 4). Fig. 2 shows the pre-segmentation of the skull in one slice of MRI data. We note that the quality of the pre-segmentation is not satisfying because of the discontinuities of the contours and of the non-segmented regions (particularly those in the vicinity of the brain). These artifacts are due in part to the coarse thresholding introduced by using s_{inf} during the region growing, and in part by not taking into account the partial volume effects that occur at the interfaces between bone and other tissues. These problems are resolved by the use of the deformable model (described in more detail below).
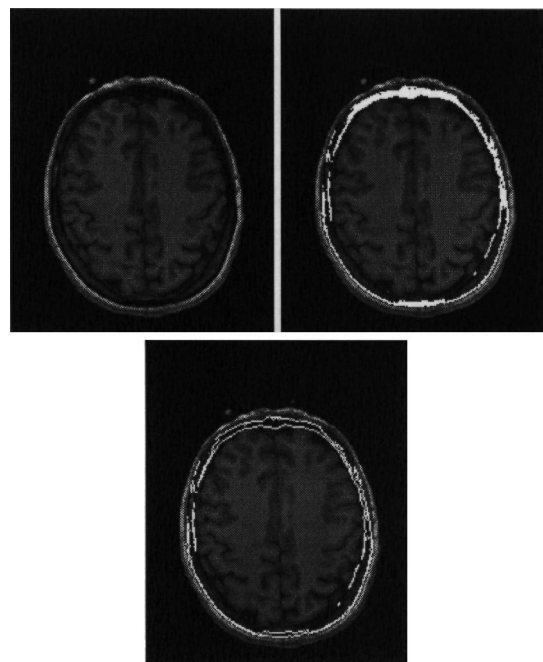
The surface of the pre-segmented region constitutes the

Fig. 2. Pre-segmentation of the skull: a slice of the MRI volume (top left). Result of the region growing (top right) with $s_{inf} = 20$. The contour of the pre-segmented region taken as an initialization of the deformable model (bottom). Obtained statistics are: $\mu_{bone} = 8.40$ and $\sigma_{bone} = 6.02$.

Fig. 1. An MRI slice and the result of the morphological segmentation of the brain. The thresholds $s_{inf} = 20$ and $s_{sup} = 125$ have been used.

automatic initialization of the deformable model. This surface is deformed by an outward propagation, in the direction of its normal. The modeling of the surface propagation must respond to the needs of our problem: the capability to effect large deformations, sub-voxel segmentation, the ability to change topology to eliminate holes and tunnels that may occur in the pre-segmented surface (these correspond to the partial volume regions that are not segmented during region growing), as well as to respond to variations between individuals. Front propagation using level set method, originally proposed by Osher and Sethian (1988), responds to these requirements. Section 3 describes this method.

2.4. General scheme for segmentation of the skull

Fig. 3 presents the stages of the method that we propose for segmenting the skull. In what follows, we present the method of front propagation using level sets, our method for estimating partial volumes, and our choices for various parameters of the model.

3. Model propagation using level set method

As mentioned above, we find the boundary of the skull by using a deformable model. The surface of the pre-segmented region, taken as the model initialization, is propagated along its normal direction using level set method.

3.1. Level set formulation

To present briefly the level set method, we follow the presentation in (Sethian, 1996). Given a closed $(N-1)$

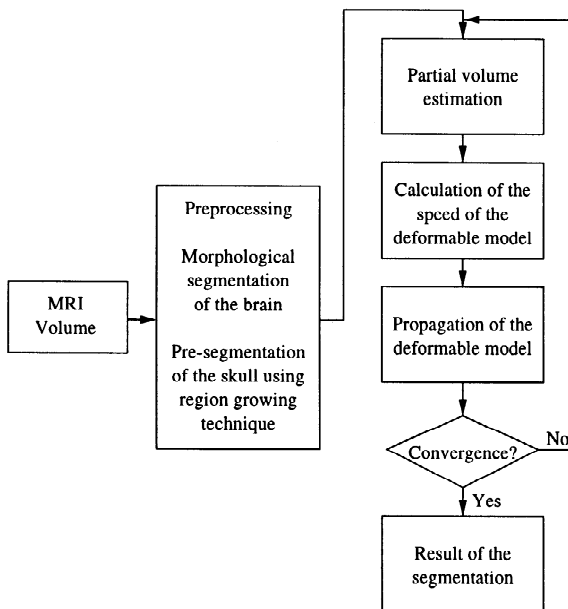Fig. 3. Stages of the skull segmentation method.

dimensional hypersurface $\gamma(t=0)$, the goal is to produce an Eulerian formulation for the motion of $\gamma(t)$ propagating along its normal direction with speed F. The main idea of the level set methodology is to embed this propagating interface as the zero level set of a function $\psi: \Re^{N} \times \Re \rightarrow \Re$ defined by

$$\psi(x, t) = \text{dist}(x, \gamma), \tag{1}$$

where $\text{dist}(x, \gamma(t))$ represents the signed distance from the point x to the front $\gamma(t)$. By definition, points inside the initial front are assigned negative distance.

The condition that moving front is the zero level set of the function ψ is expressed by the equation

$$\gamma(t) = \{x \,|\, \psi(x, t) = 0\}. \tag{2}$$

The propagation of ψ is calculated by the equation (Sethian, 1996)

$$\psi_t + F|\nabla\psi(x, t)| = 0 \quad \text{given} \quad \psi(x, t = 0), \tag{3}$$

where ψ_t is the derivative of ψ w.r.t. t, and $|\nabla\psi|$ is the norm of the spatial gradient of ψ. Eq. (3) is the Hamilton–Jacobi level set equation introduced by Osher and Sethian (1988). During the propagation of ψ, the front can always be detected using Eq. (2).

Among the several desirable aspects of this Eulerian Hamilton–Jacobi formulation, we cite:

- The evolving function $\psi(x, t)$ remains a function as long as F is smooth. However, the propagating hypersurface $\gamma(t)$ may change topology, break, merge, and form sharp corners as the function ψ evolves. In our case, this property is very important for two reasons: (i) the skull has variable topology which means that the deformable model used to segment the skull must be able to change topology; (ii) the skull presents sharp corners and complex shapes which must be segmented by the deformable model.

- Intrinsic geometric properties of the front are easily determined from the level set function ψ. Thus, at any point of the front, the normal vector is given by

$$n = \frac{\nabla\psi}{|\nabla\psi|} \tag{4}$$

and the curvature is obtained by

$$\kappa = \nabla \frac{\nabla\psi}{|\nabla\psi|}. \tag{5}$$

These geometric properties are used in the propagation process as shown in Section 4.

3.2. Numerical implementation

Because $\psi(x, t)$ remains a function as it evolves, numerical simulations of ψ propagation may be developed. Using a spatial uniform mesh with grid nodes (i, j, k) and noting that ψ_{ijk}^n is the value of ψ at point (i, j, k) at time $n\Delta t$, Eq. (3) becomes

$$\frac{\psi_{ijk}^{n+1} - \psi_{ijk}^n}{\Delta t} + (F)|\nabla_{ijk}\psi_{ijk}^n| = 0, \qquad (6)$$

where $|\nabla_{ijk}\psi_{ijk}^n|$ represents some appropriate finite difference operator for the spatial derivative. Sethian (1996) presents an extensive study about the construction of an appropriate numerical approximation of ψ spatial derivative in order to allow the formation and propagation of singularities in the front. In the one-dimensional case, it is shown in (Sethian, 1996) that an effective approximation to the gradient is given by

$$\nabla_i\psi_i = ((\max(D_i^-\psi, 0))^2 + (\min(D_i^+\psi, 0))^2)^{1/2}, \qquad (7)$$

where

$$D_i^-\psi = \frac{\psi_i - \psi_{i-1}}{\Delta i} \qquad (8)$$

and

$$D_i^+\psi = \frac{\psi_{i+1} - \psi_i}{\Delta i}, \qquad (9)$$

where Δi is the spatial step along direction i. The extensions to two- and three-dimensional cases are straightforward.

3.3. The propagation equation of our model

In our approach to segment the skull, $\gamma(t)$ evolves in 3D. $\psi^n(x, y, z)$ denotes the value of ψ at the point (x, y, z) of the space at time $n\Delta t$. The surface of the pre-segmented skull region (described in Section 2.3) is used to define the initial surface $\gamma(0)$. At each time instant $n\Delta t$, the surface $\gamma(n\Delta t)$ is calculated as the zero crossing level of the surface ψ^n.

The propagation of our model is given by

$$\psi^{n+1}(x, y, z) = \psi^n(x, y, z) + \Delta t$$
$$\cdot (-(\alpha_1 \cdot \max(F_\psi(x, y, z), 0) + \alpha_2$$
$$\cdot \min(F_\psi(x, y, z), 0)) + \varepsilon \cdot \kappa(x, y, z)), \qquad (10)$$

in which κ is the mean curvature. The term $\varepsilon\kappa$ in this equation is a smoothing term of the type classically used in deformable models. The curvature, κ, is given by

$$\kappa(x, y, z) = ((\psi_{yy} + \psi_{zz})\psi_x^2 + (\psi_{xx} + \psi_{zz})\psi_y^2$$
$$+ (\psi_{xx} + \psi_{yy})\psi_z^2 - 2\psi_x\psi_y\psi_{xy} - 2\psi_x\psi_z\psi_{xz}$$
$$- 2\psi_y\psi_z\psi_{yz})/(\psi_x^2 + \psi_y^2 + \psi_z^2)^{3/2}, \qquad (11)$$

in which ψ_x denotes the partial derivative of ψ with respect to x, and ψ_{xy} denotes the second partial derivative of ψ with respect to x and y. The remaining notation is defined analogously. The terms α_1 and α_2 are given by

$$\alpha_1 = ((\max(D_x^-\psi^n, 0))^2 + (\min(D_x^+\psi^n, 0))^2$$
$$+ (\max(D_y^-\psi^n, 0))^2 + (\min(D_y^+\psi^n, 0))^2$$
$$+ (\max(D_z^-\psi^n, 0))^2 + (\min(D_z^+\psi^n, 0))^2)^{1/2} \qquad (12)$$

and

$$\alpha_2 = ((\max(D_x^+\psi^n, 0))^2 + (\min(D_x^-\psi^n, 0))^2$$
$$+ (\max(D_y^+\psi^n, 0))^2 + (\min(D_y^-\psi^n, 0))^2$$
$$+ (\max(D_z^+\psi^n, 0))^2 + (\min(D_z^-\psi^n, 0))^2)^{1/2}. \qquad (13)$$

4. Partial volume estimation

The surface of the pre-segmented region is taken as the initialization of the deformable model. Our goal is to propagate the model until it detects the contour of the skull. Due to partial volume effects, a voxel may contain bone and tissue simultaneously. A precise segmentation implies that the deformable model must be capable of segmenting the bone part in a partial volume voxel. This means that the evolution of the model must stop when the interface between bone and tissues is reached. To achieve this goal, we calculate the speed of the model in each voxel as a function of the bone partial volume in that voxel. Thus, the model stops when the segmented part of a voxel is equal to its bone partial volume.

4.1. Background

Partial volume effects present a problem that exists for all medical imaging modalities. If a voxel corresponds to the interface between two (or several) tissues, the discrete nature of medical imaging implies that the grey level of this voxel will be the combination of the grey levels that correspond to those distinct tissues. Several approaches have been proposed in the literature for estimating the partial volume. This estimation means the determination of types and proportions of materials in each voxel of the image.

Santago and Gage (1993) calculate probability densities for the materials in the image. These probabilities are modeled with Gaussian laws fitted to the histogram of the entire volume. Materials amounts are then quantified. Once these distributions have been calculated, the proportion of each material in the partial volume voxels can be estimated.

Laidlaw et al. (1998) use a similar approach as Santago and Gage (1993) since material characterization is based on histograms. But in this approach, histograms are computed over small regions surrounding studied voxels. From these local histograms, characteristics of the classes present in each voxel are estimated by fitting Gaussians to local histograms. The local aspect of this approach better takes into account the variability of tissues in the volume.

Choi et al. (1991) use multi-channel MR images to estimate tissue proportions in each voxel of the image. In this approach, voxels are considered as a mixture of multiple tissue types and a Markov random field model is used for the classification.

Another multi-channel approach is proposed by Bonar et al. (1995). This approach uses two MRI acquisitions to segment the CSF, grey matter and white matter. Grey levels of pure tissues are determined manually in each MR image, then the proportions of pure tissues are calculated in a voxel by resolving a system of three linear equations.

Géraud et al. (1995a,b) use the fact that partial volume effect exists at interfaces between pure tissues. The proposed approach begins with a classification of the image, then tissue-labeled distance maps are calculated. These maps are used to estimate the class mean values as well as partial volume voxels. For each of these voxels, the two classes to which the voxel is closest are determined. The voxel is considered as the combination of these two classes and the voxel grey level is used to estimate its composition.

As a last example, Vincken et al. (1994) use a multi-scale approach in which each voxel, at a scale, is divided, at a finer scale, into four sub-voxels. Information propagation use voxel values as well as their neighborhood to analyze voxels at sub-voxel precision.

4.2. Characteristics of our method

The method that we propose for partial volume estimation has to be adapted to the segmentation problem we consider. Thus, the characteristics of our method can be presented by the following points:

- The results of partial volume estimation methods show that, in many cases, materials gradually degrade from one to another over many samples. However, because our aim is to detect the contour of the skull, we have to place the deformable model 'somewhere' in the transition region between bone and tissues. We chose to push the deformable model towards the region where proportions of bone and tissues are equal.
- We share the approach of Laidlaw et al. (1998) which considers a voxel as a region of the image. This consideration permits to propagate the model inside a voxel achieving a sub-voxel segmentation. In this work, we consider that a voxel is a cubic region whose volume is equal to one.
- When the deformable model propagates inside a voxel, it divides it into two zones. Our aim is to detect the zone which belongs to bone. Voxel sub-division was already proposed in (Vincken et al., 1994). However, in our approach, the direction of voxel sub-division is implied by the direction of propagation of the deformable model. This approach is different from (Vincken et al., 1994) where a voxel is always divided into four equal cubic parts.

- The global tissue characterization in the image, as proposed in (Santago and Gage, 1993), does not seem adequate in our case. In fact, several tissue types surround the skull. A local partial volume estimation, as proposed in (Laidlaw et al., 1998), is much more adapted to our problem: class characteristics are estimated in small regions around studied voxels. However, two main difficulties remain. First is the big variability of tissue grey level around the skull. This implies that grey levels of partial volume voxels between bone and tissues can cover a wide range of image grey values. This range may overlap pure tissue grey levels and makes the estimation of local pure classes characteristics difficult. The second difficulty is the existence of thin bone parts in the skull. A voxel of these parts is essentially surrounded by tissue and partial volume voxels. Pure bone class is not strongly present in the neighborhood of thin bone parts and it will not be detected by local class detection as proposed in (Laidlaw et al., 1998). This implies the risk of not estimating the pure bone proportion in voxels corresponding to these thin parts. In order to resolve these two difficulties, we estimate the partial volume in the neighborhoods of voxels which surround the deformable model. Tissue variability around the skull is detected by the spatial variability of studied neighborhoods. On the other hand, the fact that the deformable model presents the bone region in MRI volume, it is very probable that voxels in the neighborhood of the model contain bone. The presence of bone class in a voxel is then induced by the fact that the voxel is a neighbor of the model. This spatial information introduces the pure bone class in the partial volume estimation even if this class is not strongly present in the voxel neighborhood.
- We share the suggestions of (Géraud et al., 1995a,b) about the variation of image grey level when crossing from one pure tissue region to another. This idea is presented in detail in Section 4.3.1.
- We assume that the value of a partial volume voxel is a linear combination of pure class values present in the voxel. This assumption is classical in partial volume estimation approaches (Pham and Prince, 1998).

Taking these points into account, we present in what follows the partial volume estimation in voxels surrounding the deformable model. We then present the calculation of the model speed.

4.3. Partial volume estimation in the neighborhood of the model

4.3.1. Local estimation of tissue mean value

Consider a zone containing two regions: tissue (T) and bone (B) (see Fig. 4). We mean by 'tissue' all tissue other than bone in the neighborhood of bone. Grey level values of tissue and bone are M_{tissue} and M_{bone}, respectively. The
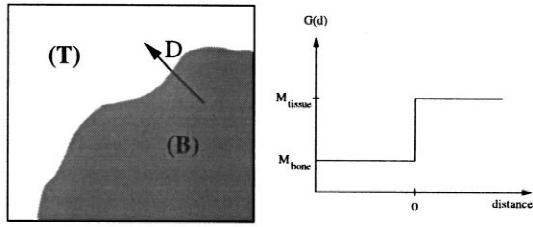
Fig. 4. Left: zone with bone (B) and tissue (T) regions. Right: grey level variation along direction D.

variation of grey level along the direction D is shown by the curve $G(d)$ in Fig. 4, where d is the signed distance to the interface between the regions (T) and (B). The curve $G(d)$ has two stable regions whose values are equal to M_{tissue} and M_{bone}, respectively. These regions correspond to zones (T) and (B). The sharp transition between the two stable regions of $G(d)$ indicates the position of the interface.

If the region of Fig. 4 is sampled (see Fig. 5). Some voxels of Fig. 5 contain bone and tissue simultaneously. In this case, the variation of grey level along D becomes as shown in Fig. 5. $G(d)$ has always two stable regions, however the transition between these regions is no longer sharp. The transition region corresponds to partial volume voxels. The interface between (T) and (B) is situated inside the transition zone.

In Fig. 5, a partial volume voxel V is divided by the interface into two regions $R_{\text{bone}}(V)$ and $R_{\text{tissue}}(V)$. The volumes of these regions are proportional to the composition $\alpha_{\text{bone}}(V)$ and $\alpha_{\text{tissue}}(V)$ in bone and tissue of the voxel V. The grey level of V is calculated by

$$g(V) = \alpha_{\text{bone}}(V) \cdot M_{\text{bone}} + \alpha_{\text{tissue}}(V) \cdot M_{\text{tissue}}. \tag{14}$$

Knowing that

$$\alpha_{\text{bone}}(V) + \alpha_{\text{tissue}}(V) = 1, \tag{15}$$

the bone composition $\alpha_{\text{bone}}(V)$ of voxel V is calculated by

$$\alpha_{\text{bone}}(V) = \frac{M_{\text{tissue}} - g(V)}{M_{\text{tissue}} - M_{\text{bone}}}. \tag{16}$$

Consider now that the grey value M_{tissue} of tissue zone is not known. It can be estimated over the stable region of
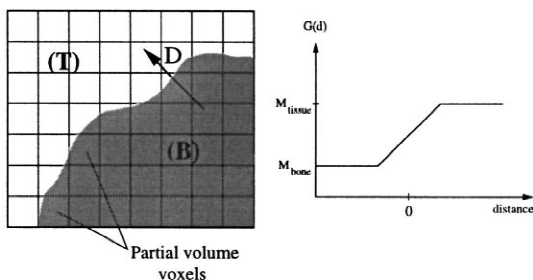
$G(d)$ situated after the transition zone. However, in real images, pure material zones are not totally homogeneous. In fact, grey level variations are caused by noise and imperfections of imagery techniques. Estimating M_{tissue} along one direction D becomes insufficient and it is necessary to use several directions in order to obtain a more robust estimation.

Consider the case of a front located in bone region as shown in Fig. 6. We can use the distance map to the front (using chamfer distance for example) to calculate the mean grey level variation of iso-distance voxels. We obtain the curve of Fig. 6. We find two stable zones corresponding to (T) and (B) and a transition region. The mean M_{tissue} of tissue class is estimated by

$$M_{\text{tissue}} = \frac{1}{N_h} \sum_i g(V_i), \quad \text{where} \quad d(V_i) > S_h, \tag{17}$$

where $d(V_i)$ is the distance of voxel V_i to the front, S_h is the distance threshold shown in Fig. 6 and N_h is the number of voxels V_i.

Suppose that the front evolves in bone region towards tissue region. Front propagation is made along its normal direction. The composition in bone α_{bone} in a region of the image reflects the probability that this region belongs to bone. When the transition region between the bone and tissue spread over several voxels, the propagating front will be attracted by the region where the interface has the biggest probability to exist. It is the region where compositions in bone and tissue are equal.

Let x_T be the position along the normal vector $\boldsymbol{n}$ where compositions in bone and tissue are equal. The speed function must attract the model toward that position. Thus the speed is calculated by

$$F(V) = -\frac{x}{x_T} + 1. \tag{18}$$

The integration of partial volume estimation and speed calculation is discussed in the next section.

4.3.2. Integration of partial volume estimation in the model propagation process

4.3.2.1. Narrow band propagation. The propagation of function ψ using Eq. (3) causes a speed definition problem. In fact, the speed in which we are interested and that we can calculate is the speed of the front γ. However, this

Fig. 5. Left: zone with bone (B) and tissue (T) regions. Right: grey level variation along direction D.
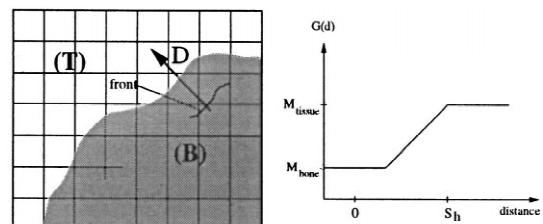

Fig. 6. Left: a front in the bone region. Right: mean grey level variation in function of the distance to the front.

speed is defined only in the domain in which γ evolves (the segmented image for example). Knowing that ψ has a higher dimensional domain than γ, the speed definition problem for all ψ levels becomes obvious. The extension of F over the entire ψ domain is necessary in order to define a speed for non zero levels of ψ. This problem was studied in detail in (Malladi et al., 1995) and two types of solutions are proposed: (i) the speed of a point in a non-zero level is considered as equal to the speed of the closest point in the zero level; (ii) the speed of a point in a non-zero level is equal to the speed of the projection of that point on the domain of γ. As indicated in (Malladi et al., 1995), the first solution permits to propagate all ψ levels without inter-level collisions. However, searching for the closest point in zero level is time consuming. The second solution may cause some levels to stop and necessitate to restrict the computation of ψ to a narrow band around the front γ. A re-initialization of ψ (using Eq. (1)) every N_{iter} iterations of Eq. (10) becomes necessary. All these problems are discussed in (Malladi et al., 1995).

We chose the second solution consisting in projecting each point of ψ in the domain of γ. Thus we obtain

$$F(\psi(x, y, z)) = F(x, y, z), \tag{19}$$

where $F(\psi(x, y, z))$ is the speed term in Eq. (10). We define two narrow bands B_1 and B_2 around γ of width $2\delta_1$ and $2\delta_2$, respectively, where $\delta_1 < \delta_2$ (see Fig. 7). Partial volume estimation uses the band B_2 and the model propagation is achieved in the band B_1.

4.3.2.2. Partial volume estimation. The partial volume estimation is integrated in the model propagation process. At each iteration, partial volume is estimated in all voxels V_i, where

$$\psi(V_i) \leq \delta_1. \tag{20}$$

For each V_i, a cylindrical neighborhood $\vartheta(V_i)$ is defined. The cylinder axis is the normal $n(V_i)$ to the front. Since V_i

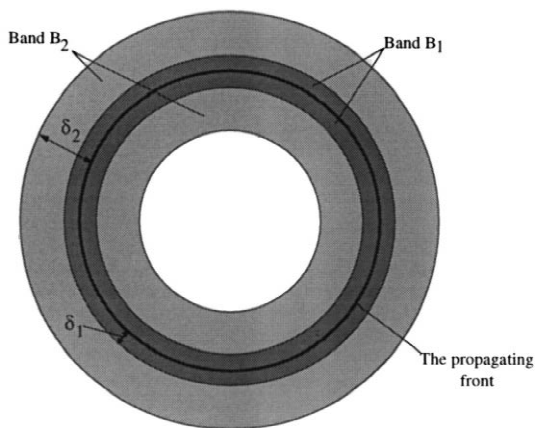is not on the model, we chose $n(V_i)$ as the normal at the closest model point to V_i. In $\vartheta(V_i)$, the variation of grey level in function of the distance to the front is calculated. Using the definition of function ψ (Eq. (1)), the value of ψ at a point is equal to the distance from this point to the front. Thus, the mean grey level at a distance d from the model is equal to

$$G(d) = \frac{1}{N_d} \sum_i v_i$$

$$\text{where} \quad v_i \in \vartheta(V_i) \quad \text{and} \quad \psi(v_i) = d, \tag{21}$$

where N_d is the number of voxels v_i. The height of the cylindrical neighborhood is equal to δ_2. This height depends on the width of tissue regions which surrounds the skull because our aim is that $\vartheta(V_i)$ reaches homogeneous tissue regions. We used a value between 7 and 9 voxels for images having about 1 mm resolution. The radius of $\vartheta(V_i)$ is selected by the user. A small radius implies that tissue mean estimation becomes sensitive to noise, while a big radius makes the estimation less local. A value of 5 voxels seems adequate for our application.

The mean value of tissues $M_{\text{tissue}}(V_i)$ in $\vartheta(V_i)$ is estimated over the stable region of $G(d)$. The bone composition of voxel V_i is calculated by

$$\alpha_{\text{bone}}(V_i) = \max\left(\frac{M_{\text{tissue}}(V_i) - g(V_i)}{M_{\text{tissue}}(V_i) - \mu_{\text{bone}}}, 0\right), \tag{22}$$

where μ_{bone} is the mean of pre-segmented region in Section 2.3. This bone composition value is used to calculate the speed of the model in voxel V_i.

4.3.2.3. Calculation of the model speed. For each point P of the deformable model, we calculate the bone composition variation $\alpha_{\text{bone}}(P)$ in band B_1 along the normal in P at the front (see Fig. 8). We then estimate the interface position along the normal where bone proportion is equal to 0.5. This means that bone and tissue proportions are equal and the interface is reached. The position x_T where the model is thus determined and the speed of the model in band B_1 is calculated using Eq. (5). However, for a good estimation of model parameters (Section 5), it is desirable

Fig. 7. Two narrow bands B_1 and B_2 of width $2\delta_1$ and $2\delta_2$ are defined around the propagating front.
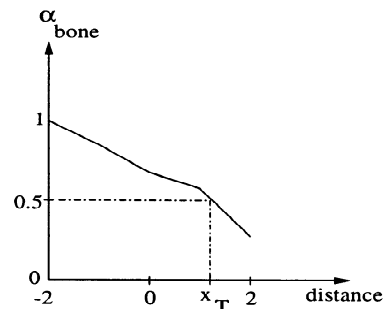

Fig. 8. The variation of bone composition along a normal vector of the model.

to have a limited speed value. We chose to limit the speed F of Eq. (5) in the interval $[-1,1]$ by using the expression,

$$\text{sign}(F) \cdot \min(|F|,1), \tag{23}$$

where $\text{sign}(\cdot)$ is the sign function. The model propagation stops when, for each point of the model, the point position and its corresponding estimated interface position x_T become stable.

4.3.3. Discussion

When deformable models are used for segmentation tasks, the image gradient is often used in order to calculate external forces which attract the deformable model. Kass et al. (1988) use the term $-|\nabla I(V)|^2$ as external potential value, where $I(V)$ is the grey level of a voxel V. In this approach, attraction force of a point of the image depends on the gradient value in that point. In order to give the same attraction potential for all gradient points of the image, Cohen et al. detect the image contours and then use chamfer distance to calculate the attraction potential (Cohen et al., 1993). Klein et al. (1997) use a bank of even and odd S-Gabor filter pairs of different orientations in order to create an external snake energy field. Lachaud and Montanvert (1996) use a tri-linear interpolation of image gradient in order to obtain a continuous potential field over the image domain and achieve a precise segmentation using deformable model. Chakraborty et al. (1996) combine image gradient with region information. The authors start with a region-based segmentation of the image. The segmentation result is introduced as an added prior into the gradient-based deformable boundary finding framework. The searched contour is defined as the curve which lies on high gradient image points and encloses a homogeneous image region. Zeng et al. (1998) use voxel grey level directly in order to attract the deformable model. In this work, class characteristics are globally defined using Gaussian laws, then the interface direction between image regions is estimated in each voxel using the membership of the voxel neighborhood to image classes. The deformable model is then attracted along the interface direction.

Our approach to calculate the model speed differs from the approaches listed above. In our problem, using image gradient to attract the model is not efficient because this technique is very sensitive to false contours caused by partial volume effect and noise. In fact, when the region to segment presents thin parts, partial volume voxels make the image gradient spread over and prevent the model from penetrating these thin parts (see Fig. 9). In addition, the gradient approach is very local and does not take into account classes which exist around the partial volume voxels. On the other hand, partial volume voxels may have the same grey level as pure tissue in the image. Calculating the speed value using voxel grey level will not be accurate in a partial volume voxel because no consideration of presented classes in the voxel is made. Moreover, this approach necessitates a global definition of class charac-

teristics. This definition is not adapted for the skull segmentation where several tissue types surround the skull.

The image shown in Fig. 9 is a synthetic image where the region (A) to segment presents sharp corners and a thin part. Region (A) is surrounded by two regions (B) and (C) of different grey values. Grey levels of the three regions are chosen such that partial volume voxels between (A) and (B) (respectively (A) and (C)) may have the same value as region (C) (respectively (B)). Fig. 9 shows segmentation results of blurred and noised images using gradient information, grey level values and our partial volume estimation approach. Segmentation was always achieved using our deformable model based on level set technique, with partial volume estimation step switched off when the two other approaches (gradient and grey level) are used. The segmentation result using partial volume
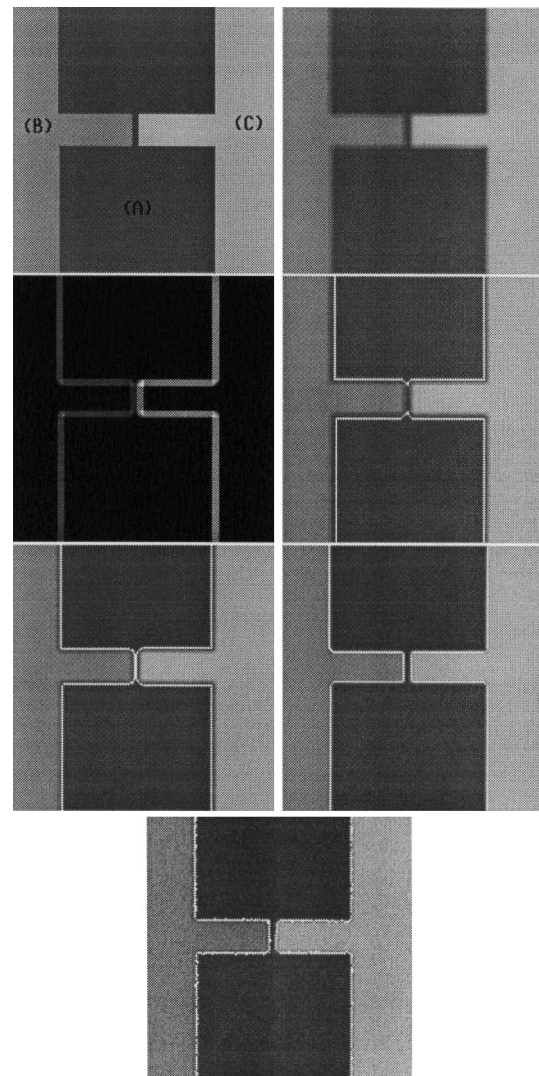

Fig. 9. From top to bottom: original image, blurred image, image gradient, contour detection using image gradient, contour detection using pixels grey levels, contour detection using partial volume estimation, blurred image with Gaussian noise added ($\sigma = 4$) and contour detection result using partial volume estimation.

estimation correctly succeeded to detect region (*A*) contour especially the contour of the thin part. The result of the gradient-based segmentation is not satisfactory in the thin part because partial volume pixels stop the model evolution. Grey level-based segmentation considers some partial volume regions (between (*A*) and (*C*)) as a part of region (*B*). These regions are not segmented by the deformable model. A global characterization of classes is insufficient is this case.

5. Determination of the model parameters

The extension of the speed function F over the domain of ψ requires the calculation of ψ in a narrow band, of width $2\delta_1$ around $\gamma(t)$ (see Section 3). The choice of the width for the band is important. This choice depends on the width of the regions in which the speed is zero (regions of tissues that surround the skull). In effect, if the width of the band is important, interfering contours may appear outside of the region to be segmented because ψ may cross zero inside and outside the segmented region (see Fig. 10).

This is due to the fact that as the width of the band increases the extension of F to points not lying on γ becomes less significant. The width of the band must then be about the minimum width of the areas in which speed is zero. In our case, we used a width $2\delta_1 = 4$ since the width of the skin and muscles around the skull exceeds 2 voxels in MRI. The function ψ is recomputed from $\gamma(t)$ every N_{iter} iterations (see Section 3). The choice of N_{iter} depends on the values of δ_1 and the time step Δt. Due to the complexity of the skull, the term which corresponds to curvature in the propagation Eq. (10) is chosen to be negligible in order to give the model the ability to develop sharp shapes. To choose these parameters, we consider that $\varepsilon = 0$. The function ψ is calculated in the narrow band of width $2\delta_1$, which implies that during the N_{iter} iterations of calculation, the front should not come out of the narrow band. According to Eq. (6) (for $\varepsilon = 0$), we have

Fig. 10. In this example, the width of the narrow band is important comparing to the width of the zone in which speed is zero. In this latter zone, the function ψ does not change: $\psi(n + k) = \psi(n)$. The computation of ψ in the narrow band makes that ψ crosses zero outside of the region to be segmented. This leads to the creation of interfering contours.
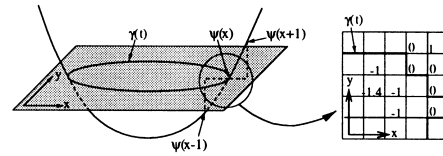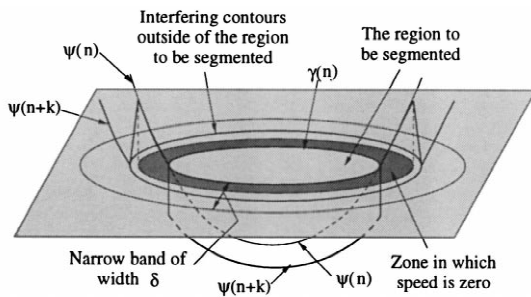

Fig. 11. Computation of α_1 and α_2: at point x, $D_x^+\psi = \psi(x + 1) - \psi(x) > 0$ and $D_x^-\psi = \psi(x) - \psi(x - 1) > 0$. We show (right) the values of ψ around $\gamma(t)$. We have: $\max(D_x^+\psi) = \max(D_x^-\psi) = 1$. The expressions of α_1 and α_2 lead to: $\max(\alpha_1) = \max(\alpha_2) = \sqrt{3}$.

$$\psi^{n+1} = \psi^n - \Delta t \cdot (\alpha_1 \cdot \max(F(x, y, z), 0)$$
$$+ \alpha_2 \cdot \min(F(x, y, z), 0)). \quad (24)$$

The front does not come out of the band during the N_{iter} iterations if

$$N_{iter} \cdot \max(\Delta t \cdot (\alpha_1 \cdot \max(F(x, y, z), 0)$$
$$+ \alpha_2 \cdot \min(F(x, y, z), 0))) < \delta_1. \quad (25)$$

Since we have $\max(|F|) = 1$ and $\max(\alpha_1) = \max(\alpha_2) = \sqrt{3}$ (see Fig. 11), we obtain

$$N_{iter} < \frac{\delta_1}{\sqrt{3}\Delta t}. \quad (26)$$

In addition, the choice of the time step Δt depends on the precision with which we wish to propagate the model. According to Eq. (1), we note that at each time step Δt, the front spatial step along its normal is

$$P = \Delta t \cdot \max(\alpha_1 \cdot \max(F(x, y, z), 0)$$
$$+ \alpha_2 \cdot \min(F(x, y, z), 0)) = \sqrt{3}\Delta t. \quad (27)$$

The spatial step P corresponds to the minimal fraction of the size of the voxel which we want to segment. This analysis resembles to that made by Cohen (1991) in the case of traditional snakes. The parameter P is fixed in advance and presents the desired precision of the segmentation.

6. Results

We tested our segmentation method on synthetic data as well as real MRI acquisitions. Synthetic data consist of simulated MRI volumes obtained by McGill University MRI simulator.[1] The simulator uses a database of 10 fuzzy volumes, each representing a class of tissues (skull, grey matter, white matter, fat, etc.) (Collins et al., 1998). The simulated MRI volume is obtained by combining these 10 volumes using different noise levels.

---

[1]Simulated MRI volumes can be downloaded from
http://www.bic.mni.mcgill.ca/brainweb/selection_normal.html

6.1. Segmentation of synthetic volumes

In order to validate the results of our method, we chose to segment the skull from simulated MRI volumes and compare the segmentation results with the skull volume in the simulator database. However, this skull volume is fuzzy, making the direct comparison with our method results (consisted of the model surface) difficult. Knowing that a voxel value in fuzzy volume is equal to the bone composition of the voxel, we used our deformable model
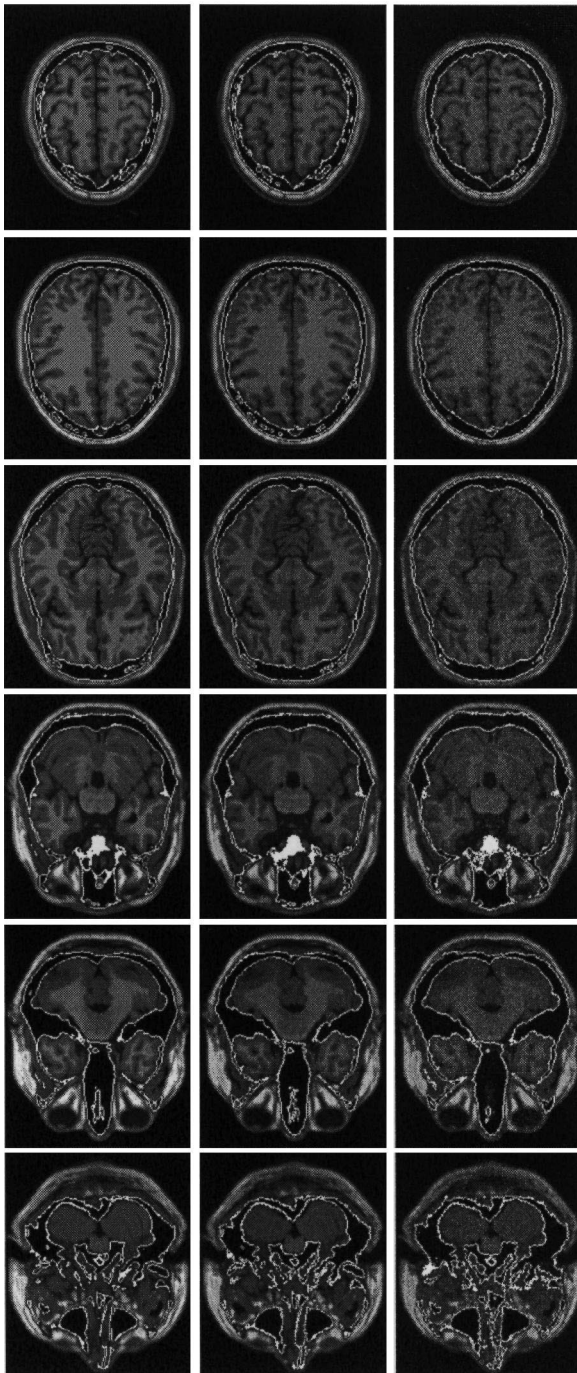

Fig. 12. Skull segmentation results in the three simulated MRI volumes: 0% noise (left), 3% noise (middle) and 9% noise (right).

to segment the skull in the fuzzy volume without estimating the partial volume (with Eq. (9)) during model propagation. We used voxel values directly as bone composition. The segmentation result is considered as the ground truth for estimating the performance of skull segmentation in simulated data.

We used our method to segment the skull in three simulated MRI-T1 weighted volumes having 0, 3 and 9% of noise level. Each volume has a size of $181 \times 217 \times 181$ voxels where a voxel has a size of $1 \times 1 \times 1$ mm. The segmentation result is compared with ground truth as follows: for each point of the segmentation result, we calculate the distance to the closest point of the ground truth. The error is equal to the mean of distances calculated for all points of the segmentation result.

We ran two tests to quantify the impact of partial volume estimation during the model propagation. In the first test, the bone composition $\alpha_{\text{bone}}(V)$ is estimated locally at each iteration as presented in Section 4. In the second test, we use the statistics calculated on the pre-segmented region (Section 2) to globally calculate the bone composition in each voxel using the function

$$\alpha_{\text{bone}}(V) = 1 \quad \text{if} \quad g(V) \leq M_{\text{bone}},$$
$$\alpha_{\text{bone}}(V) = \exp\left(\frac{(g(V) - M_{\text{bone}})^2}{\sigma_{\text{bone}}^2}\right) \quad \text{if} \quad g(V) > M_{\text{bone}}.$$

$$(28)$$

No local partial volume estimation during model propagation is realized in this test.

Fig. 12 shows segmentation results of the three synthetic volumes. In these results, partial volume is estimated during model propagation. Fig. 13 shows the error in function of iteration number for the two tests. We notice that the error is significantly less important when partial volume is locally estimated during model propagation. On the other hand, when noise level is important, error after convergence corresponds essentially to thin fatty regions in the higher parts of the skull. These regions become very hard to segment when noise is high and makes the error value increase. The segmentation differences of fatty regions among the three used volumes can be visually seen in Fig. 12.

6.2. Segmentation of real MRI volumes

We present the results of the skull segmentation in three MRI volumes, A, B and C, of different resolutions (see Table 1). The thresholds s_{inf} and s_{sup} used for the morphological segmentation of the brain are selected manually. This choice is not necessarily precise and can be made easily with an interactive thresholding tool. The width of the two narrow bands are $2\delta_1 = 4$ and $2\delta_2 = 14$, respectively, for the three segmented volumes. The value of the time step Δt depends on the precision with which we want to segment the bone. We used a spatial step $P = 0.03$ for the three volumes. The time step Δt is
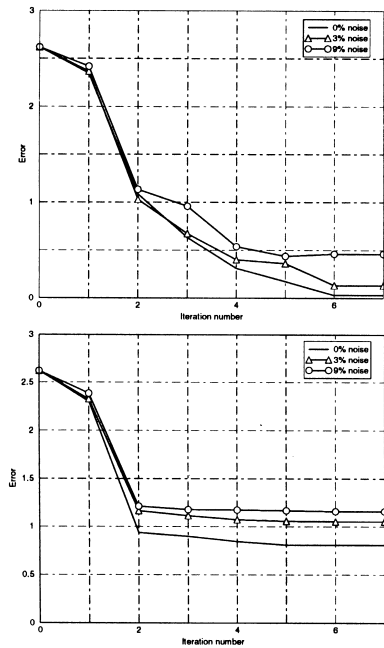
Fig. 13. Error in function of iteration number. Up: with partial volume estimation. Down: without partial volume estimation.

calculated from P and is equal to 0.02 for the three volumes. The iteration number is calculated from Δt and δ_1 (see Section 5). We used an iteration number $N_{iter} = 25$.

Figs. 14–16 show the results of segmentation of the skull of volumes A, B and C, respectively. We notice that the result of segmentation using deformable model is much better than the segmentation using region-growing technique, taken as an initialization of the deformable model (see Fig. 2). In fact, the iterative estimation of the partial volume during the propagation of the model makes it possible to carry out a precise segmentation while taking into account the local tissue variability around the skull. The deformable model is thus able to segment thin areas such as ocular globes, the higher parts of the skull as well as the jaw. Moreover, the variable topology of the deformable model enables it to segment the fatty parts of the skull and to cross them over in order to reach internal and external contours of the skull. The interindividual variability of the skull is no more a problem because no a priori topology is imposed on the model. Finally let us note that for the 3D representations, isotropic volumes were calculated by linear interpolation of the result of the segmentation. We preferred to segment original anisotropic
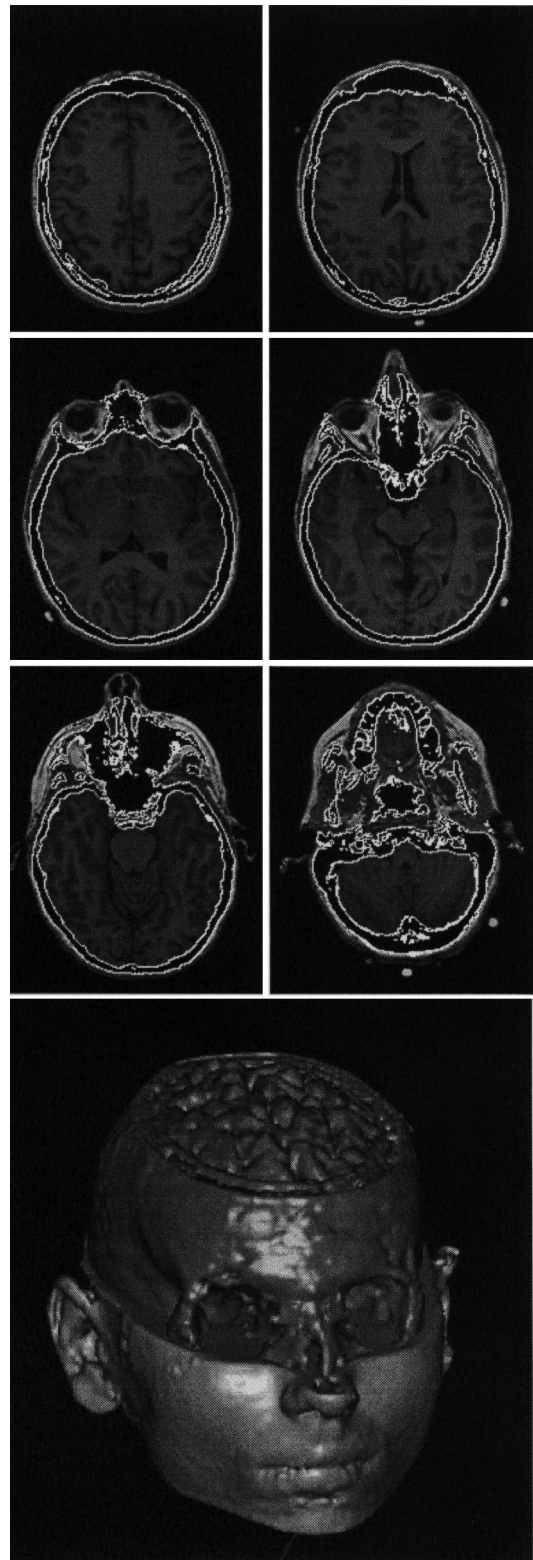
Table 1
Resolutions of the 3 MRI volumes: *nx*, *ny* and *nz* are the voxels numbers in the coronal, sagittal and axial directions, respectively. *dx*, *dy* and *dz* are the voxels dimensions (in mm) in the *x*, *y* and *z* directions

	nx	*ny*	*nz*	*dx*	*dy*	*dz*
Volume *A*	120	256	256	1.6	1	1
Volume *B*	256	256	124	1	1	1.35
Volume *C*	168	256	256	1	1	1

Fig. 14. The result of the skull segmentation of the volume A. $\delta_1 = 2$, $\Delta t = 0.02$, $\varepsilon = 0.001$. In the 3D representation, the brain is obtained by morphological segmentation, the skull is segmented using the deformable model and the remainder of the head is obtained from the original MRI volume.

Fig. 15. The result of the skull segmentation of the volume *B*. $\delta_1 = 2$, $\Delta t = 0.02$, $\varepsilon = 0.001$.

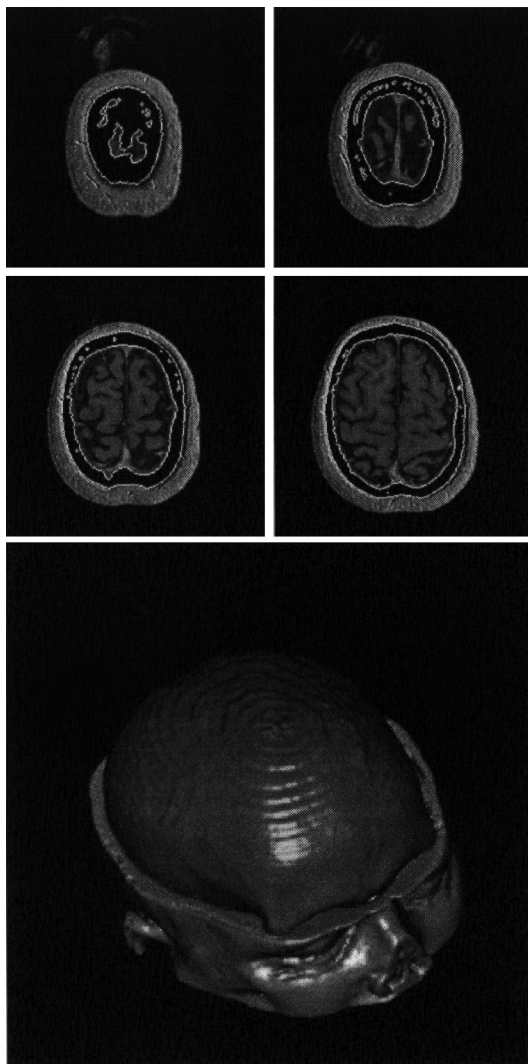Fig. 16. Coronal view of the result of the skull segmentation of the volume *C*. $\delta_1 = 2$, $\Delta t = 0.02$, $\varepsilon = 0.0001$.

tion time and the precision of the segmentation. It is to the user to choose it. In the results presented, the iteration number varies between 3 and 4, with an execution time from 35 to 40 minutes per iteration according to the size of the skull to segment. Calculation is made on a Sun Sparc, Ultra-2.

7. Conclusions

We presented a method of segmentation of the skull using a deformable model. The pre-segmentation using region-growing technique provides statistics on the bone in MRI volume as well as an automatic initialization of the deformable model. The use of level set technique makes it possible to carry out a sub-voxelic segmentation and not to impose an a priori topology on the model. The propagation speed of the model is a function of partial volume of bone which contains each voxel. The generality of the proposed approach makes it possible to adapt it to the segmentation of other anatomical structures in medical images. The method has the advantage of associating a model with high capacity of deformation with the precise calculation of the speed of the model thanks to the estimation, at each iteration, of partial volume around the model. Let us note finally that the segmentation of the skull can contribute to the automatic segmentation of other tissue of the head (skin, muscles, eyes, inner ear (Rifai et al., 1998)) by using a priori anatomical knowledge concerning the relative

volumes to avoid introducing an artificial partial volume effect due to the interpolation. The calculation time depends on the iteration number of the propagation algorithm, the size of the surface to be propagated and the time step Δt. The iteration number is strongly reduced thanks to the use of the pre-segmentation result as an initialization of the model. The region growing technique makes it possible to segment large homogeneous areas very quickly where the propagation of the deformable model takes much more time. In addition, the calculation of the surface ψ requires the calculation of distances from 3D points to the propagated surface. The calculation time is reduced by using narrow band propagation of the model. This implies that ψ is calculated only for the points belonging to the narrow bands around the propagated surface. Moreover, the calculation of the distances from these points to the surface is accelerated by the use of hashing tables. Finally, the choice of the time step Δt is a compromise between the calcula-
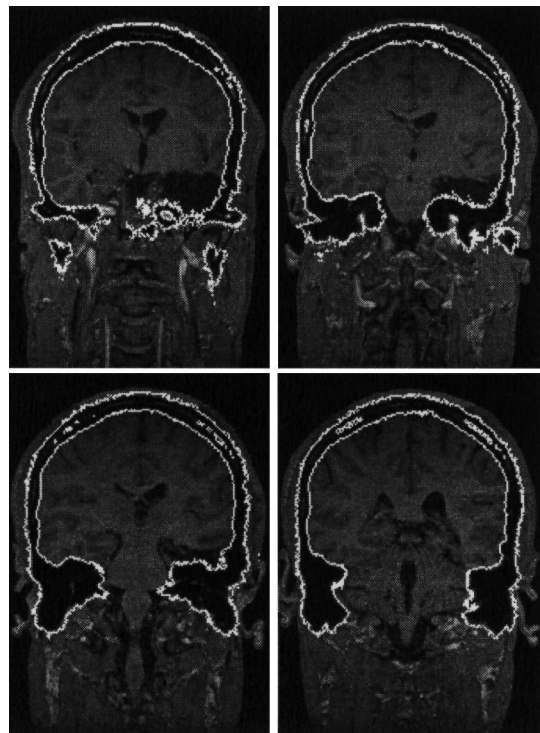
positions of these tissues with respect to the skull. The segmentation of these tissue is important for the construction of a complete realistic model of the head.

References

Bardinet, E., Cohen, L.D., Ayache, N., 1994. Fitting 3D Data Using Superquadrics and Freeform Deformations. In: 12th IEEE International Conference on Pattern Recognition (ICPR'94). Vol. A, pp. 79–83.

Caselles, V., Kimmel, R., Sapiro, G., 1977. Geodesic active contours. Int. J. of Computer Vision 22 (1), 61–79.

Chakraborty, A., Staib, L.H., Duncan, J.S., 1996. Deformable boundary finding in medical images by integrating gradient and region information. IEEE Trans. Med. Imaging 15 (6), 859–870.

Choi, H.S., Haynor, D.R., Kim, Y., 1991. Partial volume tissue classification of multichannel magnetic resonance images – a mixel model. IEEE Trans. Med. Imaging 10 (3), 395–407.

Clarysse, P., Friboulet, D., Magnin, I.E., 1997. Tracking geometrical descriptors on 3-D deformable surfaces: application to the left-ventricular surface of the heart. IEEE Trans. Med. Imaging 16 (4), 392–404.

Cohen, I., Cohen, L.D., 1994. A hybrid hyperquadric model for 2-D and 3-D data fitting. In: 12th IEEE International Conference on Pattern Recognition (ICPR'94). Vol. B, pp. 403–405.

Cohen, L.D., 1991. On active contour models and balloons. CVGIP: Image Understanding 53 (2), 211–218.

Cohen, L.D., Bardinet, E., Ayache, N., 1993. Surface reconstruction using active contour models. In: Conference on Geometric Methods in Computer Vision. Vol. 2031, pp. 38–50, SPIE.

Collins, D.L., Zijdenbos, A.P., Kollokian, V., Sled, J.G., Kabani, N.J., Holmes, C.J., Evans, A.C., 1998. Design and construction of a realistic digital brain phantom. IEEE Trans. Med. Imaging 17 (3), 463–468.

Davatzikos, C., Bryan, R.N., 1996. Using a deformable model to obtain a shape representation of the cortex. IEEE Trans. Med. Imaging 15 (6), 785–795.

Fok, Y.L., Chan, J.C.K., Chin, R.T., 1996. Automated analysis of nerve-cell images using active contour models. IEEE Trans. Med. Imaging 15 (3), 353–368.

Gee, J., Reivich, M., Bajcsy, R., 1993. Elastically deforming 3D atlas to match anatomical brain images. J. Comput. Assist. Tomogr. 17 (2), 225–236.

Géraud, T., Aurdal, L., Maître, H., Bloch, I., Adamsbaum, C., 1995a. Estimation of Partial Volume Effect Using Spatial Context. Application to Morphometry in Cerebral Imaging. In: IEEE Medical Imaging Conference, San Francisco, CA, October 1995.

Géraud, T., Mangin, J.F., Bloch, I., Maître, H., 1995b. Segmenting internal structures in 3D MR images of the brain by Markovian relaxation on a watershed based adjacency graph. In: IEEE International Conference on Image Processing ICIP-95. pp. 548–551.

Heinonen, T., Eskola, H., Dastidar, P., Laarne, P., Malmivuo, J., 1997. Segmentation of T1 MR scans for reconstruction of resistive head models. Comput. Methods Programs Biomed. 3 (54), 173–181.

Held, K., Kops, E.R., Krause, B.J., Wells, W.M., Kikinis, R., MullerGartner, H.W., 1997. Markov random field segmentation of brain MR images. IEEE Trans. Med. Imaging 16 (6), 878–886.

Jensen, M.A., Rahmat-Samii, Y., 1995. EM interaction of handset antennas and a human in personal communications. IEEE Proc. 83 (1), 7–17.

Kass, M., Witkin, A., Terzopoulos, D., 1988. Snakes: active contour models. Int. J. of Computer Vision 1 (4), 321–331.

Klein, A.K., Lee, F., Amini, A.A., 1997. Quantitative coronary angiography with deformable spline models. IEEE Trans. Med. Imaging 16 (5), 468–482.

Lachaud J.O., Montanvert A., 1996. Volumetric segmentation using hierarchical representation and triangulated surface. In: European Conf. on Computer Vision 96. Vol. 1064, pp. 137–146.

Laidlaw, D.H., Fleischer, K.W., Barr, A.H., 1998. Partial volume bayesian classification of material mixtures in MR volume data using voxel histograms. IEEE Trans. Med. Imaging 17 (1), 74–86.

Lobregt, S., Viergever, M.A., 1995. A discrete dynamic contour model. IEEE Trans. Med. Imaging 14 (1), 12–24.

Malladi, R., Sethian, J.A., Vemuri, B.C., 1995. Shape modeling with front propagation: a level set approach. IEEE PAMI 17 (2), 158–175.

Mangin, J.F., 1995. Mise en correspondance d'images médicales 3D multi-modalités multi-individus pour la corrélation anatomo-fonctionnelle cérébrale. PhD thesis, ENST-E010.

Marin, G., 1997. Utilisation de la méthode des éléments finis pour le calcul des champs électromagnétiques à l'aide d'un modèle réaliste de tête en MEG et EEG. PhD thesis Université PARIS XI.

McInerney, T., Terzopoulos, D., 1996. Deformable models in medical image analysis: a survey. Medical Image Analysis 1 (2), 91–108.

Meijs, J.W.H., Bosch, F.G.C., Peters, M.J., Lopes da Silva, F.H., 1987. On the magnetic field distribution generated by a dipolar current source situated in a realistically shaped compartment model of the head. Electroencephalogr. Clin. Neurophysiol. 66, 286–296.

Osher, S., Sethian, J.A., 1988. Fronts propagating with curvature dependent speed: algorithms based on Hamilton-Jacobi formulation. J. Comput. Phys. 79, 12–49.

Pham, D.L., Prince, J.L., 1998. Partial volume estimation and the fuzzy c-means algorithm. In: IEEE International Conference on Image Processing ICIP-98. pp. 819–822.

Rifai, H., Bloch, I., Wiart, J., Garnero, L., Dormont, D., 1998. Segmentation, suivi, modélisation 3D et recalage de l'oreille interne à partir de données IRM. RFIA 3, 71–80.

Rueckert, D., Burger, P., Forbat, S.M., Mohiaddin, R.D., Yang, G.Z., 1997. Automatic tracking of the aorta in cardiovascular MR images using deformable models. IEEE Trans. Med. Imaging 16 (5), 581–590.

Santago, P., Gage, H., 1993. Quantification of MR brain images by mixture density and partial volume modeling. IEEE Trans. Med. Imaging 12 (3), 566–574.

Sethian, J.A., 1996. In: Level Set Methods. Cambridge University Press, Cambridge.

Soltanian-Zadeh, H., Windham, J.P., 1997. A multiresolution approach for contour extraction from brain images. Med. Phys. 12 (24), 1844–1853.

Staib, L., Duncan, J., 1992. Boundary finding with parametrically deformable models. IEEE Trans. PAMI 14 (11), 1061–1075.

Studholme, C., Hill, D.L.G., Hawkes, D.J., 1996. Automated 3-D registration of MR and CT images of the head. Medical Image Analysis 1 (2), 163–175.

Subsol, G., 1995. Construction automatique d'atlas anatomiques morphométriques à partir d'images médicales tridimentionnelles. PhD thesis, Ecole centrale de Paris.

Vincken, K., Koster, A., Viergever, M., 1994. Probabilistic segmentation of partial volume voxels. Pattern Recognition Lett. 15 (5), 477–484.

Wehli, F.W., Shaw, D., Kneeland, J.B., 1988. In: Biomedical Magnetic Resonance Imaging: Principles, Methodology and Applications. VCH, Weinheim.

Wiart, J., Mittra, R., 1996. Calculation of the Power Absorbed by Tissues in Case of Hand Set Mobile Antenna Close to Biological Tissue. IEEE APS, Baltimore, MD.

Zeng, X., Staib, L.H., Schultz, R.T., Ducan, J.S., 1998. Segmentation and measurement of the cortex from 3D MR images. In: MICCAI'98, pp. 519–530.